Structure
Article

Full-Length Structure of a Sensor Histidine Kinase Pinpoints Coaxial Coiled Coils as Signal Transducers and Modulators

Ralph P. Diensthuber,[1,*] Martin Bommer,[2,3] Tobias Gleichmann,[1] and Andreas Möglich[1,*]
[1]Biophysikalische Chemie
[2]Strukturbiologie/Biochemie
Institut für Biologie, Humboldt-Universität zu Berlin, 10115 Berlin, Germany
[3]Helmholtz-Zentrum Berlin für Materialien und Energie, BESSY-II, AG Makromolekulare Kristallographie, Albert-Einstein-Straße 15, 12489 Berlin, Germany
*Correspondence: ralph.diensthuber@hu-berlin.de (R.P.D.), andreas.moeglich@hu-berlin.de (A.M.)
http://dx.doi.org/10.1016/j.str.2013.04.024

SUMMARY

Two-component systems (TCSs), which comprise sensor histidine kinases (SHK) and response-regulator proteins, represent the predominant strategy by which prokaryotes sense and respond to a changing environment. Despite paramount biological importance, a dearth exists of intact SHK structures containing both sensor and effector modules. Here, we report the full-length crystal structure of the engineered, dimeric, blue-light-regulated SHK YF1 at 2.3 Å resolution, in which two N-terminal light-oxygen-voltage (LOV) photosensors are connected by a coiled coil to the C-terminal effector modules. A second coaxial coiled coil derived from the N-termini of the LOV photosensors and inserted between them crucially modulates light regulation: single mutations within this coiled coil attenuate or even invert the signal response of the TCS. Structural motifs identified in YF1 recur in signal receptors, and the underlying signaling principles and mechanisms may be widely shared between soluble and transmembrane, prokaryotic, and eukaryotic signal receptors of diverse biological activity.

INTRODUCTION

Excitability, i.e., the ability to perceive and respond to signals, is a basic hallmark of life. Two-component systems, which comprise sensor histidine kinase (SHK) and cognate response regulator (RR), are the most widespread and important signal transduction systems in prokaryotes but also occur in certain eukaryotes, notably in *Saccharomyces cerevisiae* and *Arabidopsis thaliana* (Gao and Stock, 2009; Capra and Laub, 2012). Sensor histidine kinases commonly consist of an N-terminal stimulus-specific sensor module and a C-terminal effector module, which comprises the *d*imerization/*h*istidine *p*hosphotransfer (DHp) and *c*atalytic/*A*TP-binding (CA) domains. Most sensor histidine kinases catalyze three distinct phosphotransfer reactions: autophosphorylation at the eponymous histidine residue within the DHp domain and both phosphorylation and dephosphorylation of the cognate RR; certain SHKs apparently lack the phosphatase activity (Gao and Stock, 2009). While the sensor modulates all three elementary reactions, the biological response is determined by net kinase activity, i.e., the balance between antagonistic phosphorylation and dephosphorylation of the RR (Russo and Silhavy, 1993).

SHKs exhibit remarkably diverse combinations of sensor and effector modules (Finn et al., 2006; Aravind et al., 2010), which is particularly evident for the two most frequently occurring two-component system (TCS) signaling modules, HAMP (Hulko et al., 2006) and Per-ARNT-Sim (PAS) domains (Szurmant et al., 2007; Möglich et al., 2009b). The plethora of combinatorial arrangements affords immense functional versatility and arguably accounts for the wide recurrence of TCS. Although it is unclear whether SHKs employ universal signal transduction mechanisms, to some extent, these mechanisms are evidently shared, as certain sensor and effector modules are functionally exchangeable. In particular, we previously replaced the oxygen-sensitive PAS-B domain of the *Bradyrhizobium japonicum* FixL SHK with the flavin-mononucleotide (FMN)-binding light-oxygen-voltage (LOV) photosensor domain from *Bacillus subtilis* YtvA (Figure 1A; Möglich et al., 2009a). The resultant, engineered SHK YF1 phosphorylates its cognate RR FixJ with near-FixL activity in the dark; however, upon blue-light absorption, a covalent bond forms between the FMN chromophore and cysteine 62 within the LOV sensor (Christie et al., 1998; Herrou and Crosson, 2011), and YF1 phosphatase activity is enhanced, which results in a more than 1,000-fold decrease of net kinase activity.

High-resolution structures of isolated sensor (Gao and Stock, 2009), DHp (Tomomori et al., 1999), and CA (Bilwes et al., 1999) domains have greatly contributed to elucidating the molecular architecture of SHKs. Two landmark crystal structures of the entire effector module from the *Thermotoga maritima* SHK HK853 (Marina et al., 2005; Casino et al., 2009) revealed that the DHp and CA domains are connected by flexible hinges and thus can adopt different spatial orientations (Albanesi et al., 2009), depending on functional state. Arguably due to this flexibility, full-length SHKs containing both sensor and effector modules have so far largely eluded structural characterization. The mechanism by which the signal is transmitted from the sensor

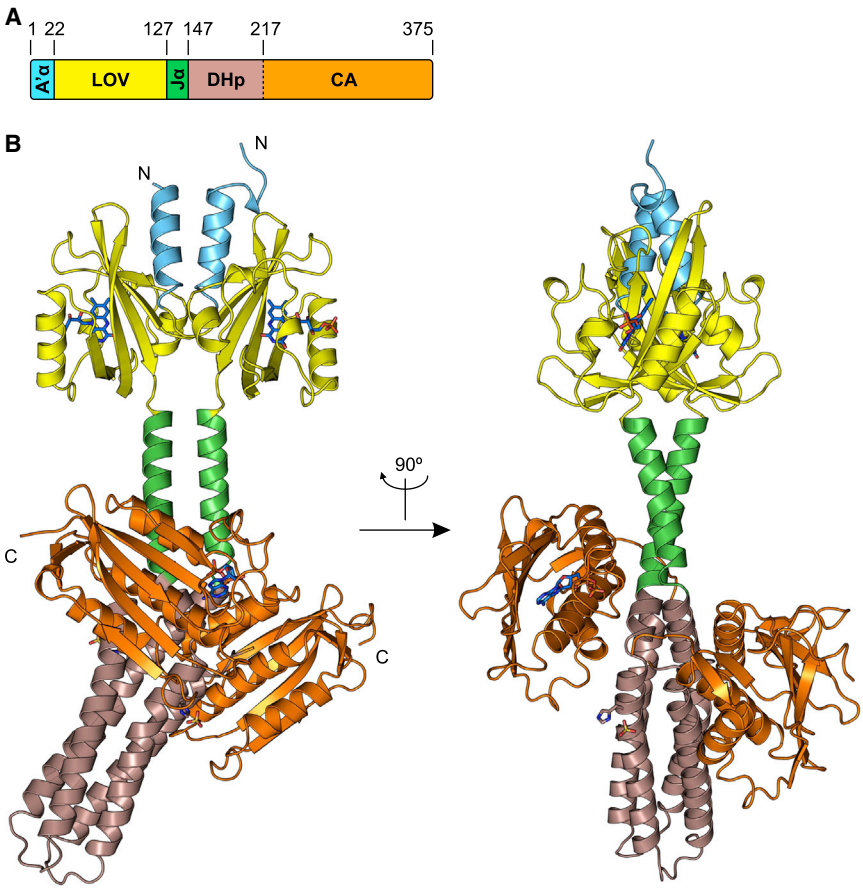

Figure 1. Crystal Structure of YF1

(A) Domain architecture of YF1. A′α (aa 1–22) in blue, LOV domain (aa 23–127) in yellow, Jα linker (aa 128–147) in green, DHp domain (aa 148–217) in rose, and CA domain (aa 218–375) in orange.

(B) The crystal structure of dark-adapted YF1. FMN cofactors within the LOV domains, residues H161 and nearby sulfate ions within the DHp domain, and ADP within the CA domain of monomer A are shown in stick representation; domain coloring as in (A).

Figure S1 shows crystal packing and an electron density omit map of the FMN binding pocket. See also PDB Session S1.

to the effector modules, in particular, the precise molecular nature of the connection between sensor and effector, has thus remained unclear. Only during the review of this manuscript, the structure of the VicK SHK, comprising both sensor and effector moieties, has been reported (Wang et al., 2013).

We now report the crystal structure of the sensor histidine kinase YF1 at full length. Via site-directed mutagenesis, we identify residues that govern signal response and net kinase activity and that can be modified to reprogram the properties of the TCS (e.g., to invert its response to signal).

RESULTS

Structure of the Blue Light-Regulated Histidine Kinase YF1

Crystals of native and selenomethionine-substituted YF1 were obtained by sitting-drop vapor diffusion in the dark in space group $P6_522$ and diffracted X-rays to 3.1 and 2.3 Å resolution, respectively. The structure of YF1 was solved by molecular replacement, confirmed by selenium single-wavelength anomalous dispersion, and refined at 2.3 Å resolution to R_{work} = 17.87% and R_{free} = 21.70% (Table 1). Within each asymmetric unit, two YF1 molecules assemble into an elongated, parallel dimer, which comprises 4,420 Å^2 of solvent-accessible surface area (Figure 1B). The dimer interface is formed by an intricate α-helical spine, which traverses the entire molecule and consists of three segments. An N-terminal parallel coiled coil (denoted A′α; amino acids [aa] 9–22) is inserted into the interface between the two LOV domain cores (aa 23–127). Coaxial with the A′α coiled coil, the C-terminal Jα helices of the LOV domain (aa 128–147) form a second coiled coil that is contiguous with N-terminal helices of the DHp domains (aa 148–217), which dimerize as an antiparallel four-helix bundle (Tomomori et al., 1999). A pronounced kink of ~35° within the N-terminal region of the DHp domain probably arises from intermolecular packing within the YF1 crystal lattice (Figure S1A available online). Notably, the globular LOV photosensor and CA domains (aa 218–375) are situated laterally to the helical spine and make no direct contact with each other.

The two LOV domains adopt the characteristic PAS fold (Crosson and Moffat, 2001; Möglich et al., 2009b), which comprises a five-stranded antiparallel β sheet (strands Aβ, Bβ, Gβ, Hβ, and Iβ) and four α helices (Cα, Dα, Eα, and Fα). The absence of a covalent bond between the FMN and C62 confirms that YF1 assumes its fully dark-adapted state (Figure S1B). When crystallized as a truncated construct (aa 20–147) lacking the additional, N-terminal A′α helix (Möglich and Moffat, 2007), the same LOV domain showed closely similar tertiary structure but differences in the dimer interface. In the YF1 structure, the A′α helices assemble into a coiled coil at the LOV-domain interface and are stabilized by interactions among the hydrophobic residues I9, L13, I16, and L20 and by mostly intermolecular contacts with the β sheets of the adjacent LOV domains (Figures 2A and S2). Prominently, the aliphatic side chains of V15 and A19 protrude into a hydrophobic cavity lined by V27 and I29 in strand Aβ, M111 and I113 in strand Hβ, and by Y118 and V120 in strand Iβ. In contrast to these hydrophobic, nondirectional interactions, the C terminus of A′α is precisely oriented by a pair of intra- and intermolecular hydrogen bonds to the adjacent LOV domains. Residue D21 forms an intramolecular hydrogen bond to the backbone of residue Q44 within helix Cα, and H22 forms an intermolecular hydrogen bond with residue D109 within strand Hβ of the opposite LOV domain. The junction between the LOV domain and the C-terminal Jα helix is provided by the conserved

Table 1. Data Collection and Refinement Statistics

Data Collection	SeMet	Native
Space group	$P6_522$ (179)	$P6_522$ (179)
Cell Dimensions		
a, *b*, *c* (Å)	105.16, 105.16, 441.80	105.14, 105.14, 443.57
α, β, γ (°)	90, 90, 120	90, 90, 120
Resolution (Å)	47.51–2.30 (2.44–2.30)[a]	50.00–3.07 (3.25–3.07)
R_{sym} (%)	7.4 (49.9)	11.8 (54.5)
I/σ_I	18.7 (3.7)	22.3 (4.8)
Completeness (%)	99.8 (99.0)	99.8 (99.0)
Redundancy	6.4 (6.2)	10.6 (10.8)
Refinement	SeMet	
Resolution (Å)	47.51–2.30	
No. reflections	121,322	
R_{work}/R_{free} (%)	17.87/21.70	
No. Atoms		
Protein	5,794	
Ligand/ion	139	
Water	451	
B-Factors (Å^2)		
Protein	45.6	
Ligand/ion	82.4	
Water	50.0	
Root-Mean-Square Deviations		
Bond lengths (Å)	0.008	
Bond angles (°)	1.141	
Ramachandran plot	98.66% favored; 1.34% allowed	
TLS groups	monomer A: 8–126, 127–217, 218–373	
	monomer B: 2–126, 127–217, 218–380	

[a]Highest resolution shell is shown in parentheses.

residues D125, I126, and T127 (DIT motif; Möglich et al., 2009a), which are engaged in five hydrogen bonds with each other and the backbone of W103 in strand Hβ (Figures 2B and S2). Thus precisely coordinated, the Jα helices form a coiled coil via hydrophobic interactions of their C-termini (L136, L139, L143, and V146), whereas their N-termini are splayed apart. As the Jα helices are conjoined with helices of the DHp domain, a continuous α-helical linker is established between the LOV photosensor and effector modules of the YF1 SHK.

The DHp domain comprises two long helices α1 (aa 148–181) and α2 (aa 189–214) that are connected by a short hairpin (aa 182–188) in clockwise direction, also found in EnvZ (Tomomori et al., 1999), but different from the counterclockwise direction in HK853 (Marina et al., 2005; Casino et al., 2009; Figures S3A and S3B). In both YF1 monomers, the phosphoaccepting histidine 161 complexes a sulfate ion via its Nδ atom, which is thought to mimic phosphorylation (Marina et al., 2005); the YF1 structure may thus represent a pseudoautophosphorylated state of the SHK. The C-terminal CA domains adopt the canonical mixed αβ sandwich fold (Bilwes et al., 1999) and are attached to the DHp domains by unstructured loops (Figure 3). Due to the clockwise orientation of the DHp helices, the CA domains are in closer proximity to the phosphoaccepting residues H161 within the opposite monomer than to those within the same monomer, which argues for autophosphorylation in *trans* (Casino et al., 2009). Although the YF1 crystals were grown in the presence of excess ATP, only the CA domain of monomer A binds ADP via residues within the conserved N, F, G1, and G2 sequence regions (Parkinson and Kofoid, 1992; Figure S3C). In monomer B, the nucleotide-binding loop (aa 310–337) adopts a divergent conformation, in which residues D318 and M335 obstruct the nucleotide-binding pocket and residues T329, T330, and K331 point outward (Figure S3D). The difference in nucleotide binding between monomers A and B is accompanied by partial unwinding of the α2 helix within the DHp domain of monomer B and by an altered orientation of their CA domains relative to the DHp domains (Figure 3). While the CA domains largely occupy equivalent regions in space, they are rotated by ~58.7° and translated by 3.5 Å relative to another. The distance between the ADP cofactor (atom Pβ) in monomer A to H161 (atom Nδ) in monomer B amounts to 23.0 Å; a comparable distance of 21.8 Å between the ADP nucleotide and the phosphoaccepting histidine is found in the structure of HK853, which undergoes autophosphorylation in *cis* (Marina et al., 2005; Casino et al., 2009). When modeling an ADP nucleotide into the binding pocket of the CA domain in monomer B of YF1, a distance of 12.8 Å is obtained to the phosphoaccepting H161 of monomer A (Figure 3B). A similar CA orientation and ADP-histidine distance (12.9 Å) are observed in the complex structure of HK853 and its response regulator (Protein Data Bank [PDB] 3DGE; Casino et al., 2009). The orientation of the CA domain in monomer B of YF1 may thus be predisposed to binding the response regulator and subsequent steps. While it is difficult to confidently ascribe functional states to the two CA conformations and orientations presently observed in the YF1 structure, they at least demonstrate the inherent flexibility of SHKs.

Coiled Coils as Key Modulators of Signal Transduction

A survey of diverse PAS domains suggested that signal transduction generally originates in structural changes within the central β sheet and concomitant modulation of the affinity between the outer face of the sheet and its interacting partner(s), which frequently is (are) an α helix (Möglich et al., 2009b). In particular, in the monomeric LOV2 domain from *Avena sativa* phototropin 1 (AsLOV2), the C-terminal Jα helix packs on the outer face of the β sheet (Halavaty and Moffat, 2007); blue-light absorption leads to a weakening of this interaction and to dissociation and unfolding of Jα (Harper et al., 2003). Intriguingly, A′α of YF1 is in a location equivalent to that of Jα in AsLOV2, although A′α derives from the juxtaposed LOV domain and runs in the opposite direction (Figure S5). To test the notion that A′α is involved in signal transduction, we generated mutants of YF1 and measured their activity and dependence on light using the pDusk-DsRed plasmid (Ohlendorf et al., 2012). Briefly, this plasmid encodes YF1 and its cognate RR FixJ, which drive expression of the fluorescent reporter DsRed in *Escherichia coli*, thus allowing facile measurements of net kinase activity (Figure 4A). In the reference construct YF1, blue-light absorption results in 10.3-fold decreased fluorescence compared to dark conditions. To ascertain that the in vivo fluorescence observed in the pDusk background indeed reflects the activity of YF1 variants, we compared the levels of intracellular, soluble protein of these variants to

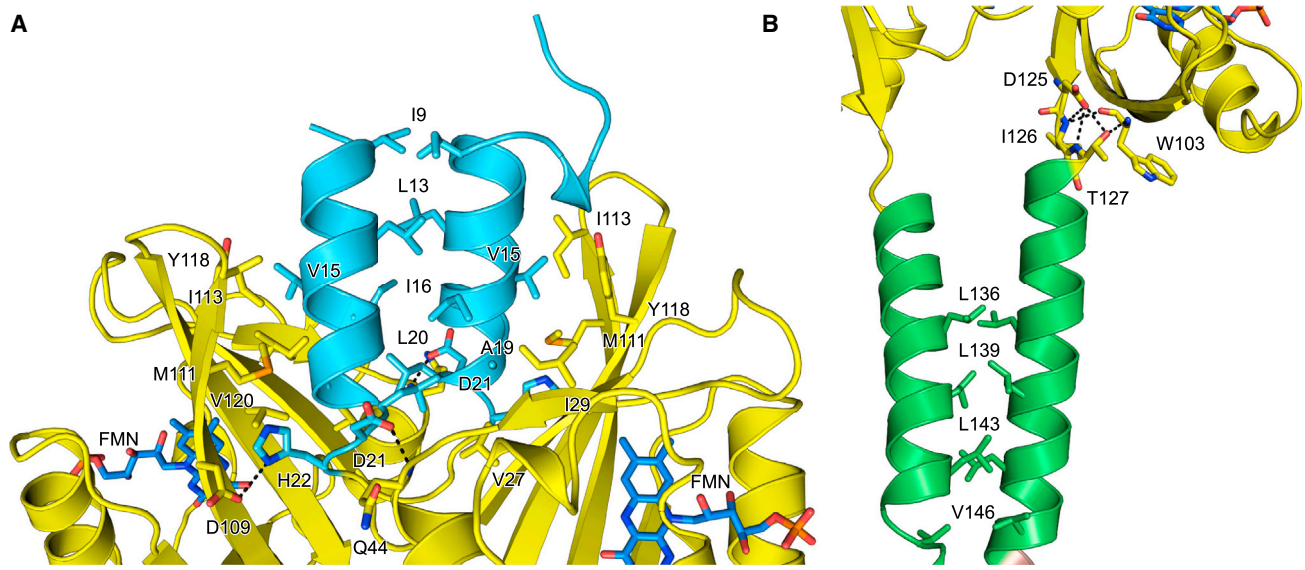

Figure 2. The A′α and Jα Coiled Coils

(A) The N-terminal A′α coiled coil. The A′α helices are engaged in hydrophobic interactions among I9, L13, I16, and L20 and numerous, mostly intermolecular contacts to the adjacent LOV domains. Residues V15 and A19 within A′α protrude into a hydrophobic cavity lined by V27, I29, M111, I113, Y118, and V120 within the juxtaposed LOV β sheet. At the C terminus of A′α, residue D21 forms an intramolecular hydrogen bond to the backbone of Q44 and residue H22 forms an intermolecular hydrogen bond to D109.

(B) The C-terminal Jα coiled coil. The Jα helices display hydrophobic interactions among L136, L139, L143, and V146. Residues D125, I126, and T127 within the DIT motif at the base of Jα form five hydrogen bonds with each other and with the backbone of W103 in strand Hβ of the LOV domain.

Figure S2 presents an extended view of the LOV β sheet and helices A′α and Jα.

wild-type YF1 by western blotting (Figures 4B and S4). All YF1 variants shown in Figure 4A were expressed to similar or at most slightly lower extent as the wild-type.

Mutations within A′α of hydrophobic residues that mediate the coiled coil interaction either attenuated light responsiveness (L13A) or completely abolished activity, as in the case of I16A,

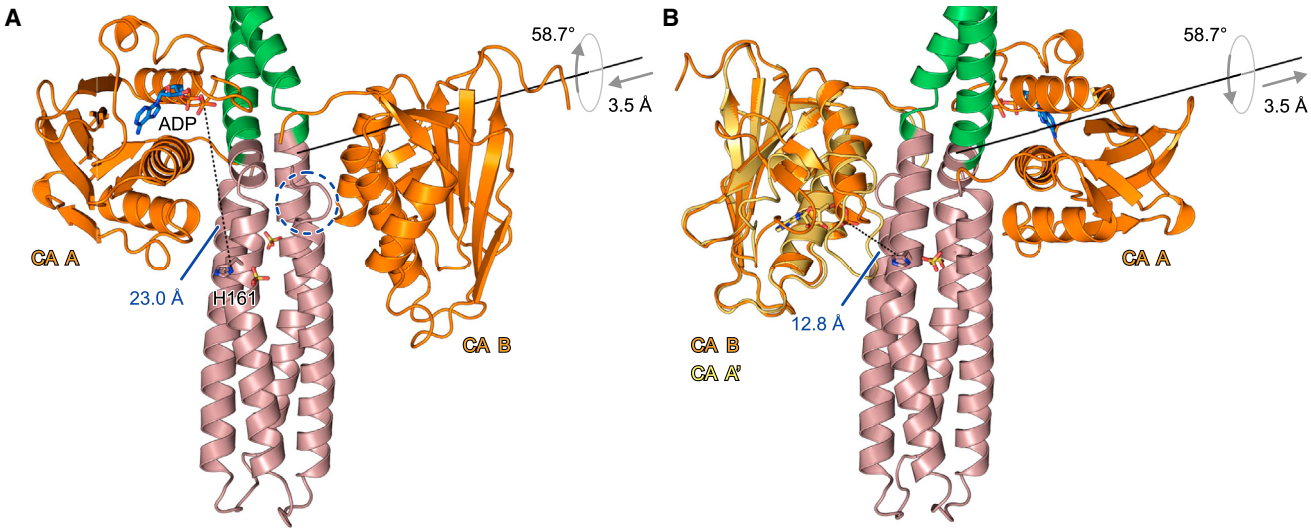

Figure 3. Orientation of the DHp and CA Domains

(A) The distance from the ADP cofactor (atom Pβ) within the CA domain of monomer A to the phosphoaccepting histidine 161 (atom Nδ) of monomer B is 23.0 Å (dashed line). The CA domain of monomer B occupies a similar spatial position relative to the DHp domain, but its angular orientation differs. The positions and orientations of the CA domains A and B relative to the DHp domains are related by a 58.7° rotation around and 3.5 Å translation along the screw-rotation axis indicated (solid line). The dashed circle highlights partial unwinding of the α2 helix of the DHp domain in monomer B.

(B) Nucleotide binding in the CA domain of monomer B was modeled by superposing a copy of the ADP-binding CA domain of monomer A (light orange, denoted CA A′). In this model, the distance between ADP and H161 is only 12.8 Å. The views of YF1 in (A) and (B) are aligned with respect to the α1 and α2 DHp helices of monomers A and B, respectively.

(A) and (B) of Figure S3 compare the architecture of the DHp domains in YF1 to that in HK853 (Marina et al., 2005); (C) and (D) show close-up views of the YF1 CA domains of monomer A and B.

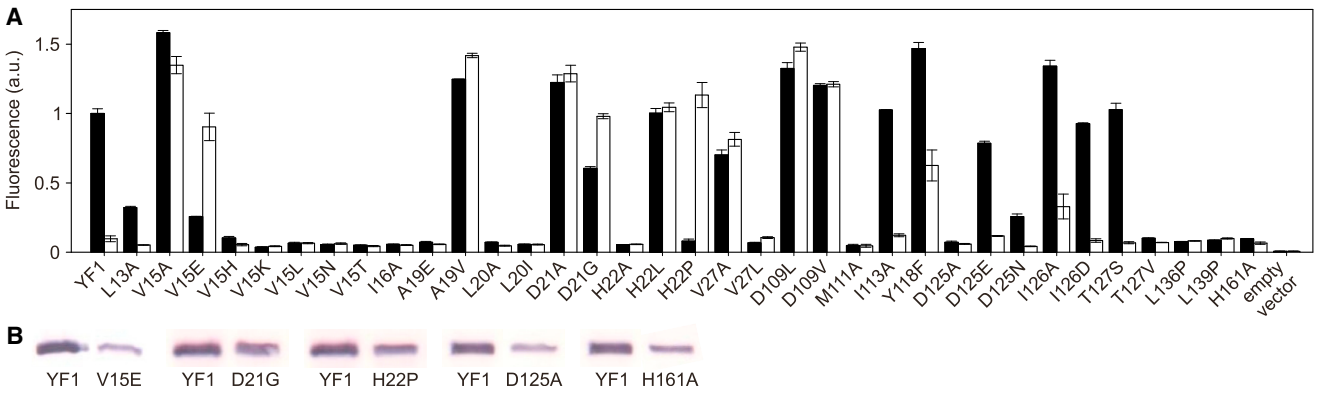

Figure 4. Activity and Light Regulation of YF1 Variants

(A) Mutants of YF1 were tested for activity using the pDusk system, in which YF1 and FixJ drive expression of the fluorescent reporter DsRed in a light-regulated manner (Ohlendorf et al., 2012). For YF1, fluorescence indicative of net kinase activity is reduced by 10.3-fold under blue light (white bars) in comparison to dark conditions (black bars).

(B) Expression levels of YF1 variants in the pDusk context were monitored by western blotting. As exemplarily shown for selected variants, all YF1 mutants shown in (A) were expressed to similar extent as wild-type.

Data represent mean ± SD of biological triplicates. Western blotting data for all YF1 mutants are reported in Figure S4.

L20A, and L20I. Replacement of residues V15 and A19 by other aliphatic residues (V15A and A19V) largely removed light responsiveness and resulted in constitutive activity. By contrast, the nonconservative mutations V15H, V15K, V15N, V15T, and A19E abolished activity. Interestingly, introduction of glutamate at position 15 inverted the signal response: blue light no longer decreased but rather enhanced activity by 3.5-fold. Variation of residues within the LOV β sheet that interact with V15 and A19 either abolished activity (V27L and M111A) or impaired light responsiveness (V27A and Y118F). Disruptions by mutagenesis of the hydrogen bonds formed by residues D21 and H22 at the C terminus of A′α have profound effects on light regulation and activity. Whereas the mutations D21A, H22L, D109L (Avila-Pérez et al., 2009), and D109V resulted in constitutive activity, the variants D21G and H22P displayed inverted signal responses with 1.6-fold and 14.3-fold enhanced activity in the light in comparison to the dark. Taken together, these data pinpoint the A′α coiled coil as a crucial modulator that governs how input signals are converted into changes of output activity: single mutations within A′α suffice to abolish, to attenuate, or even to invert the signal response of the TCS system.

We extended our mutational analysis to the junction between the LOV sensors and the Jα coiled coil, which the YF1 structure identifies as the sole connector between the spatially well-separated sensor and effector modules. Removal of hydrogen bonds at this junction in D125A and T127V abolished activity, whereas retention of hydrogen-bonding capability, as in D125E, D125N, and T127S, largely retained activity and light responsiveness. Mutations of I126 are relatively well tolerated and merely led to moderate impairment of light responsiveness (I126A and I126D). The mutagenesis data corroborate the pivotal role of the DIT motif at the interface between LOV sensors and Jα coiled coil, since removal of even a single hydrogen bond suffices to abrogate activity. Proper signal transduction crucially depends on the integrity of the Jα helix, as evidenced by the introduction of helix-breaking proline residues (L136P and L139P) that disrupted activity. We propose that, in marked contrast to AsLOV2, the Jα helices in YF1 provide a rigid conduit, along which signals are propagated from sensor to effector over extended molecular distances, presumably as quaternary structural changes (Matthews et al., 2006; Möglich et al., 2009b).

DISCUSSION

Structure-Informed Model for Signal Transduction

We previously proposed the rotary-switch mechanism, which posits that signals are propagated from sensor to effector as torque movements within a coiled coil linker (Möglich et al., 2009a). In support of this model, the YF1 structure now reveals a continuous helical spine, which provides an axle around which rotary motions may occur. Crucially, the axes of the A′α and Jα coiled coils are precisely aligned, which is conducive to transmitting torque motions between them and to the C-terminal effector module. Additional coiled coils could serially concatenate and coaxially align additional N-terminal sensor domains, thereby providing the structural rationale for signal integration in multi-input signal receptors (Möglich et al., 2010). A molecular model for signal transduction in YF1 is now afforded by comparison to the structure of the *Pseudomonas putida* LOV protein SB1 (Circolone et al., 2012). While SB1 lacks a C-terminal effector module, it shares with YF1 high sequence similarity (41.7% identity within aa 25–127 of YF1) and a similar overall fold; crucially, SB1 was crystallized in its fully light-adapted state. Thus, we generated a homology model for the light-adapted state of the YF1 LOV photosensor on the basis of the SB1 structure and compared it to the experimentally determined dark-adapted structure (Figure 5; Movies S1 and S2). In the framework of this model, the LOV domains would rotate upon light absorption by about 15° around the axes indicated in Figure 5A (solid lines); remarkably, the swivel point for this rotation is at the interface between the LOV β sheet and the A′α coiled coil, which our functional data identify as a hub for signal modulation. The A′α helices would tilt and thereby increase their crossing angle from 29° in the dark-adapted state to almost 70° in the light-adapted state.

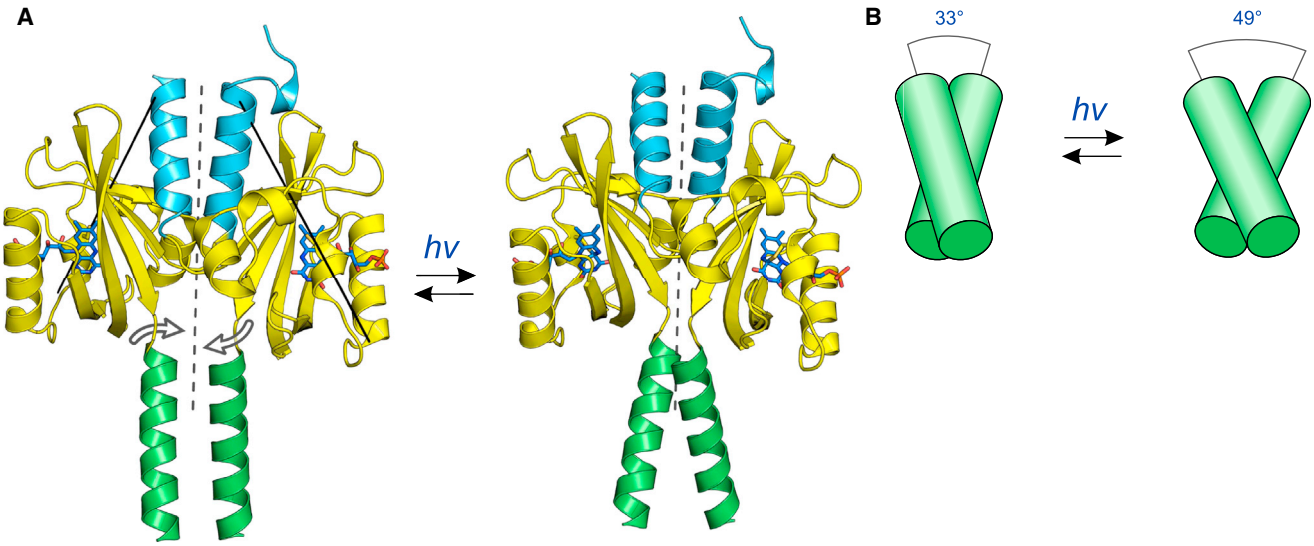

Figure 5. Structure-Based Model for Signal Transduction

(A) The YF1 LOV photosensor domains in their dark-adapted state as determined by x-ray crystallography (left) are compared to a homology model of their light-adapted state (right), based on the structure of the *Pseudomonas putida* SB1 LOV protein (Circolone et al., 2012). Light absorption could induce quaternary structural rearrangements that culminate in a supertwist of the C-terminal coiled coil (arrows). Structures were aligned with respect to the LOV core domains (residues 25–126). The dimer axis is shown as a dashed line; screw-rotation axes describing the motions of the LOV core domains are shown as solid lines.

(B) Light absorption could increase the crossing angle of the Jα helices from 33° to 49°, thus increasing the left-handed supertwist of the coiled coil. Figure S5 shows conserved modes of interaction between the β sheet of LOV domains and flanking helices. Movies S1 and S2 show an animation of the signal-transduction model depicted in (A).

The quaternary structural transition of the LOV domains would further entail a rotation of the C-terminal Jα helices around the dimer axis and a concomitant increase of their crossing angle from 33° in the dark-adapted state to 49° in the light-adapted state. The increase of the helix-crossing angle would in turn induce left-handed torque and lead to a supertwisting of the left-handed Jα coiled coil. Notably, the rotary-switch mechanism we propose is compatible with two recent models for signal transduction in SHKs. In the model advanced by Coles, Lupas, and colleagues (Ferris et al., 2012), signals would induce rotary movements within the antiparallel coiled coil of the DHp domain, akin to the torque motions we implicate for YF1; resultant subtle structural rearrangements would modulate the interaction between DHp and CA domains and thus regulate net kinase activity. The helix-cracking model (Dago et al., 2012) envisions signal-induced structural perturbations, which lead to partial unfolding of helix α2 of the DHp domain, as we indeed observe in monomer B of our structure (Figure 3); as a consequence, the mobility of the CA domain would be enhanced, enabling it to associate with and phosphorylate the active-site histidine. Our structure, our functional data, and the rotary-switch mechanism are consistent with both models, and we thus cannot discriminate between them. In fact, the two models are not in contradiction, and signal transduction may well rely on aspects of both. Whereas our data implicate torque movements in signal transduction from sensor to effector, in other SHKs, evidence for piston-type movements has been obtained (Cheung and Hendrickson, 2009; Falke and Erbse, 2009; Moore and Hendrickson, 2009). Apparently, multiple and ingenious mechanisms are at play in the regulation of SHKs and other signal receptors.

Recurring Motifs in Signal Receptors

YF1, although an engineered SHK, is representative of diverse naturally occurring signal receptors (Finn et al., 2006), including numerous PAS-linked (cf. Figure 5 of Möglich et al., 2009a) and LOV-linked (Purcell et al., 2007; Swartz et al., 2007) species. Notably, the structural principles evidenced in the photoreceptor YF1 also apply to the prevalent transmembrane chemoreceptors: helices and coiled coils corresponding to Jα traverse the plasma membrane and thereby connect the physically separated extracellular (or periplasmic) sensor and intracellular effector modules. Indeed, helix rotation has been implicated in the signal transduction of certain transmembrane SHKs (Hulko et al., 2006) and signal receptors (Moukhametzianov et al., 2006). The architecture of YF1 recurs in diverse signal receptors, including the transmembrane SHK CitA (Sevvana et al., 2008) and soluble bacteriophytochrome red-light sensors (Yang et al., 2008; Figures 6 and S6). Although the molecular details somewhat differ, in all cases, sensor domains interact through their β sheets with a central α-helical spine that connects to a C-terminal effector module. Intriguingly, these similarities are limited neither to SHKs nor to prokaryotes, as evidenced by the recent structure of the heterodimeric complex of the transcription factors CLOCK and BMAL1 (Huang et al., 2012) from mouse (Figures 6 and S6). Despite their eukaryotic provenance and a different effector module, consisting of an N-terminal helix-loop-helix domain, the PAS-A domains of CLOCK and BMAL1 embrace a coiled coil highly reminiscent of A′α in YF1. In line with the structural resemblance, certain mutations of residues in the interface between the PAS-A domains of BMAL1 and CLOCK lead to functional impairment (Huang et al., 2012). Thus, structural principles identified in YF1 are widely shared across

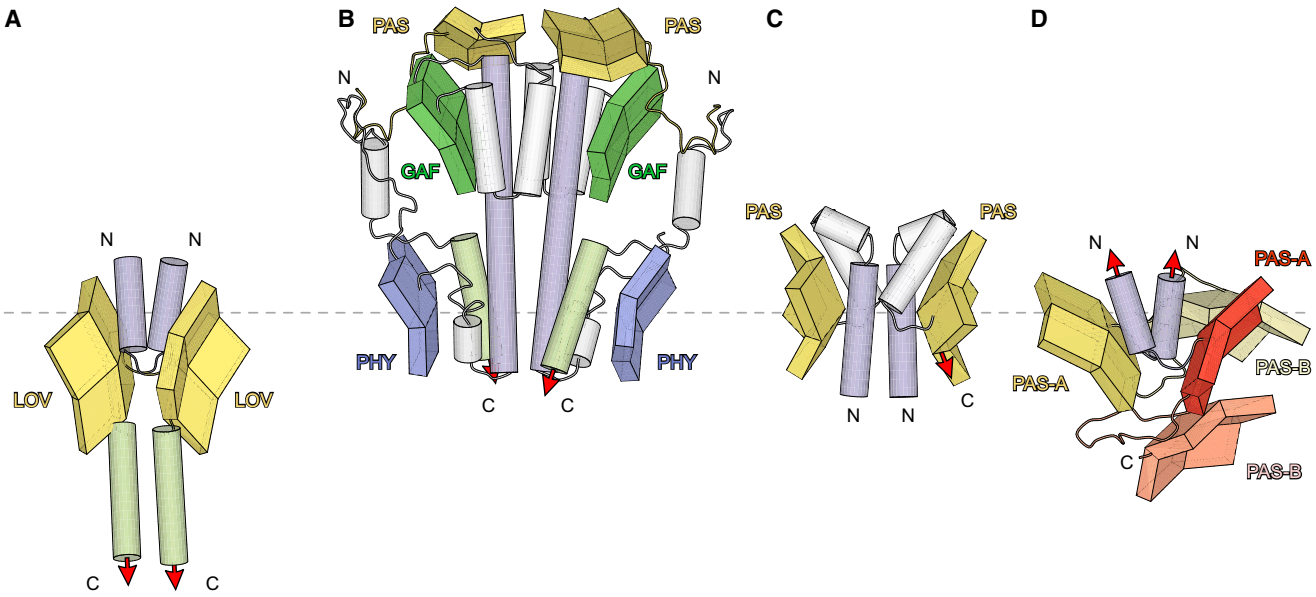

Figure 6. Recurring Structural Motifs in Signal Receptors

(A) A schematic of the YF1 LOV photosensor domains (yellow shapes) and the A′α and Jα coiled coils (blue and green cylinders). Signals may be propagated as rotary movements within the Jα helices to the C-terminal effector modules (red arrows).

(B–D) Closely related structural configurations with sensor domains embracing coiled coils corresponding to A′α are widely observed in diverse signal receptors (e.g., in bacteriophytochrome red-light sensors [(B), *Pseudomonas aeruginosa* BphP (Yang et al., 2008)], in bacterial chemoreceptors [(C), *Klebsiella pneumoniae* CitA (Sevvana et al., 2008)], and in the mouse CLOCK:BMAL1 complex [(D) (Huang et al., 2012)]). Notably, in contrast to the other receptors, CLOCK and BMAL1 form a heterodimer are of eukaryotic origin and have N-terminal helix-loop-helix effector modules.

Figure S6 shows the four structures of signal receptors in cartoon representation.

homodimeric and heterodimeric, soluble and transmembrane, single-input and multi-input, and prokaryotic and eukaryotic signal receptors that combine disparate sensor and effector modules in different topologies (N→C versus C→N). We suggest that the structural correspondence entails similar signaling mechanisms.

Helical connectors (Anantharaman et al., 2006), coiled coils, and signal-induced quaternary structural changes (e.g., rotary switching) represent versatile concepts (Möglich et al., 2009b) that enable the combination of various sensor and effector modules and could at least partially account for the enormous diversity of such combinations found in nature (Finn et al., 2006). The YF1 structure confirms that coiled coils obviate the need for direct contact or shape complementarity between sensors and effectors. The design of novel sensor-effector combinations—be it by evolution (Capra and Laub, 2012), be it by rational engineering—thus greatly simplifies to correctly fusing α helices and coiled coils, which link sensor and effector modules. Moreover, since even single mutations within the sensor (e.g., H22P in YF1) suffice to completely alter the signal response of receptors at the physiological level, environmental stimuli can be rapidly rewired to achieve a novel cellular adaptation.

EXPERIMENTAL PROCEDURES

Molecular Biology and Protein Expression

The gene encoding YF1 was amplified by PCR from an earlier expression construct in the pET-28c vector (Möglich et al., 2009a). Ligation into the pET-41a expression vector (Novagen, Merck) via restriction sites *NdeI* and *XhoI* yielded the plasmid pET-41a-YF1, in which YF1 is furnished with a C-terminal octahistidine affinity tag. The reporter plasmid pDusk-myc-DsRed was derived from the plasmid pDusk-DsRed (Ohlendorf et al., 2012) via PCR by appending a *myc* epitope (EQKLISEEDL) to the C terminus of YF1. Site-directed mutants of YF1 were generated in the background of the reporter plasmid pDusk-myc-DsRed according to the QuickChange protocol (Invitrogen, Life Technologies). The identity of all constructs was confirmed by DNA sequencing (GATC Biotech).

For protein expression, pET-41a-YF1 was transformed into *E. coli* BL21 CmpX13 cells (Mathes et al., 2009). A 5 ml overnight culture was used to inoculate 500 ml Luria broth (LB) media containing 50 μg ml^{-1} kanamycin and 50 μM riboflavin. Cells were grown at 37°C and 225 rpm to an optical density at 600 nm (OD_{600}) of 0.6, at which point expression was induced with 1 mM isopropyl β-D-1-thiogalactopyranoside (IPTG). After incubation for 4 hr at 37°C and 225 rpm, cells were harvested by centrifugation and resuspended in 20 ml buffer A (50 mM Tris-HCl pH 8.0, 20 mM NaCl, 20 mM imidazole, protease inhibitor cocktail Complete Ultra [Roche Diagnostics]). Cells were lysed by sonication, and the suspension was cleared by centrifugation. The supernatant was loaded on a 5 ml Ni^{2+}-chelate affinity column (GE Healthcare) using an ÄKTAprime plus chromatography system (GE Healthcare) and washed with ten column volumes (CV) buffer A followed by ten CV buffer B (50 mM Tris-HCl pH 8.0, 1 M NaCl). His_8-tagged YF1 protein was eluted from the resin with an imidazole gradient from 20 mM to 1 M imidazole over 12 CV. Fractions containing pure YF1 were identified on the basis of analysis by polyacrylamide gel electrophoresis and pooled. After dialysis against twice 2 l buffer C (10 mM Tris-HCl pH 8.0, 10 mM NaCl, 10% [v/v] glycerol), the protein solution was concentrated in a 10,000-molecular weight cutoff spin concentrator (Pall Corporation) to ~40 mg ml^{-1} and stored at −80°C. Protein concentration was determined with an Agilent 8453 UV-visible spectrophotometer (Agilent Technologies) using an extinction coefficient of 12,500 M^{-1} cm^{-1} at 450 nm (Möglich et al., 2009a).

Selenomethionine-substituted (SeMet) YF1 protein was produced as described (Doublié, 1997). Briefly, CmpX13 cells containing pET-41a-YF1

were grown in 500 ml M9 minimal media supplemented with 50 μg ml^{-1} kanamycin, 50 μM riboflavin, 0.4% (w/v) glucose, 0.1 mM $CaCl_2$, 2 mM $MgSO_4$, and 1 mg l^{-1} thiamine. Protein expression was induced at OD_{600} of 0.6 by adding 1 mM IPTG, 100 mg l^{-1} each of the L-amino acids isoleucine, leucine, lysine, phenylalanine, threonine, and valine, and 60 mg l^{-1} selenomethionine. Protein purification was performed as described above.

Crystallization and Data Collection

Crystals of native YF1 were grown by sitting-drop vapor diffusion in the dark. One microliter of a solution containing 40 mg ml^{-1} YF1, and 1 mM ATP/$MgCl_2$ in buffer C was mixed with 1 μl reservoir solution (0.1 M potassium fluoride, 2 M $(NH_4)_2SO_4$). Multilayered, hexagonal crystals of up to 300 μm appeared after several days of incubation at 18°C. Immediately before rapid cryocooling in liquid nitrogen, crystals were soaked in cryoprotection solution (0.1 M potassium fluoride, 2 M $(NH_4)_2SO_4$, 25% [v/v] glycerol). Crystallization of SeMet YF1 was conducted under the same conditions but yielded thick, coin-shaped single crystals of up to 300 μm diameter.

Monochromatic oscillation X-ray diffraction data were collected at 100 K and a wavelength of 0.9184 Å for both native and SeMet samples on beamline 14.1 at the BESSY II electron storage ring (Berlin-Adlershof) (Mueller et al., 2012), which is operated by the Helmholtz-Zentrum Berlin. Native crystals of YF1 diffracted X-rays to 3.07 Å resolution and were indexed in space group $P6_522$ (*179*) with unit cell dimensions of $a = b = 105.14$ Å and $c = 443.57$ Å. SeMet YF1 crystals diffracted X-rays to 2.30 Å resolution and were also indexed in space group $P6_522$ (*179*) with slightly different unit cell dimensions of $a = b = 105.16$ Å and $c = 441.80$ Å. Indexing, integration, and scaling were performed with the XDS program (Kabsch, 2010) through the XDSAPP interface (Krug et al., 2012).

Structure Determination and Analysis

We first solved the structure of YF1 on the basis of the native diffraction data by molecular replacement (MR). Search models for the DHp and CA domains were derived from structures of *T. maritima* HK853 (Marina et al., 2005; Casino et al., 2009; PDB 3DGE and 2C2A, respectively) with the CHAINSAW program (Stein, 2008). Using the PHASER software (McCoy et al., 2005), two monomers of the isolated *B. subtilis* YtvA LOV domain (PDB 2PR5, aa 26–127) (Möglich and Moffat, 2007), one copy of the DHp search model, and two copies of the CA search model were placed within the unit cell. Initial refinement of the MR solution yielded *R*-factors of R_{work} = 44.32% and R_{free} = 48.83%. For calculation of R_{free}, 5.0% of reflections across all resolution shells were randomly assigned and used only for validation. Based on the resulting electron density, the structure was automatically rebuilt with the BUCCANEER (Cowtan, 2012) program from the CCP4 suite (Winn et al., 2011). When diffraction data from SeMet YF1 crystals became available, the MR solution was confirmed by selenium single-wavelength anomalous dispersion (Sheldrick, 2008).

Model building was done with COOT (Emsley and Cowtan, 2004); structure refinement was initially done with Refmac5 (Murshudov et al., 1997) and at later stages with PHENIX (Adams et al., 2002). The final model was obtained by restrained B-factor and *t*ranslation *l*ibration *s*crew-motion (TLS) (Schomaker and Trueblood, 1968) refinement against the 2.3 Å SeMet data. To account for incomplete incorporation of selenomethionine, the occupancies of the selenium atoms were individually optimized during refinement. Electron density could be resolved for residues 8–373 of monomer A and residues 2–218 and 220–375 of monomer B. Five additional residues deriving from the vector and the C-terminal His_8-tag are also resolved in monomer B. The *R*-factors are R_{work} = 17.87% and R_{free} = 21.70%; other data collection and refinement statistics are provided in Table 1. The structure was validated with tools included in COOT and with MOLPROBITY (Chen et al., 2010), which yielded an "All-Atom Clashscore" of 6.96 (98th percentile for resolution range 2.30 ± 0.15 Å) and a "MolProbity score" of 1.66 (98th percentile). All residues lie within either the favored (98.66%) or allowed (1.34%) regions of the Ramachandran plot. Omit maps (Figure S1B) were obtained with PHENIX by removing atoms of the FMN chromophores and of the side chain of C62 from the final model followed by simulated-annealing refinement.

The model for the light-adapted state of YF1 was generated in two steps on the basis of the crystal structure of *P. putida* SB1 (Circolone et al., 2012; PDB 3SW1). First, the LOV domains, including the A′α helices (aa 1–126) of monomers A and B of YF1 were superposed as rigid bodies on the matching regions (aa 1–119) of SB1 using LSQKAB (Kabsch, 1976). Second, the Jα helices (aa 127–147) of YF1 were separately superposed on the corresponding helices (aa 120–134) of SB1. Although side chain rotamers were not optimized, the resultant model for the light-adapted state of YF1 is largely devoid of steric clashes.

Buried surface area within the YF1 dimer was determined using the PISA web server (Krissinel and Henrick, 2007). Atomic coordinates and structure-factor amplitudes have been deposited in the Protein Data Bank under accession number 4GCZ. Molecule graphics were prepared with PyMOL (Schrödinger; Figures 1, 2, 3, 5, S1–S3, and S5; Movies S1 and S2) and MOLSCRIPT (Kraulis, 1991; Figures 6 and S6).

Activity Assays

Site-directed mutants of YF1 in the pDusk-myc-DsRed background were transformed into *E. coli* BL21 CmpX13. Three 5 ml LB cultures each were incubated overnight at 37°C and 225 rpm, either in the dark or under constant blue light (100 μW cm^{-2}). DsRed fluorescence and OD_{600} were measured with a Tecan M200 plate reader (Tecan Group) in 96 well μClear plates (Greiner BioOne), as described (Ohlendorf et al., 2012). Fluorescence excitation and emission wavelengths were set at 554 ± 9 nm and 591 ± 20 nm, respectively. Data were normalized to the fluorescence observed for YF1 under dark conditions and represent the averages of three biological replicates ± SD.

Expression of YF1 and its mutants within the pDusk-myc-DsRed background was confirmed by western blotting. The cell pellet from 1 ml of above bacterial culture was lysed by addition of the nonionic detergent B-PER according to the manufacturer's protocol (Thermo Fisher Scientific). The amount of B-PER was normalized to OD_{600} of the cell cultures to achieve equal concentrations of solubilized protein. After removal of insoluble debris by centrifugation, the supernatant was separated by SDS-PAGE and analyzed by western blotting using anti-c-*myc* primary and alkaline phosphatase-conjugated anti-rabbit immunoglobulin G secondary antibodies (Sigma-Aldrich).

ACCESSION NUMBERS

The Protein Data Bank accession number for the coordinates and structure-factor amplitudes reported in this paper is 4GCZ.

SUPPLEMENTAL INFORMATION

Supplemental Information includes six figures, two movies, and one PDB session file and can be found with this article online at http://dx.doi.org/10.1016/j.str.2013.04.024.

ACKNOWLEDGMENTS

We are indebted to Dr. H. Dobbek for advice, discussion, and provision of crystallization facilities. We thank Dr. P. Hegemann, Dr. M. Kolbe, Dr. B. Martins, Dr. K. Moffat, and members of the Möglich laboratory for advice and discussion. We appreciate support during data collection at BESSY. The project was funded through a Sofja-Kovalevskaya Award by the Alexander-von-Humboldt Foundation (to A.M.) and by the Cluster of Excellence in Catalysis (Unicat). M.B. is supported by Humboldt-Universität zu Berlin through the Joint Berlin MX program.

R.P.D. and A.M. conceived the project and designed experiments. R.P.D. carried out molecular biology, protein purification, crystallization, collection of diffraction data, structure determination, and activity assays. M.B. participated in crystallization, collection of diffraction data, and structure determination. T.G. discovered and analyzed several mutant variants of YF1. A.M. supervised the study. R.P.D. and A.M. interpreted data and wrote the manuscript.

Received: March 1, 2013
Revised: April 15, 2013
Accepted: April 30, 2013
Published: June 6, 2013

REFERENCES

Adams, P.D., Grosse-Kunstleve, R.W., Hung, L.W., Ioerger, T.R., McCoy, A.J., Moriarty, N.W., Read, R.J., Sacchettini, J.C., Sauter, N.K., and Terwilliger, T.C. (2002). PHENIX: building new software for automated crystallographic structure determination. Acta Crystallogr. D Biol. Crystallogr. *58*, 1948–1954.

Albanesi, D., Martín, M., Trajtenberg, F., Mansilla, M.C., Haouz, A., Alzari, P.M., de Mendoza, D., and Buschiazzo, A. (2009). Structural plasticity and catalysis regulation of a thermosensor histidine kinase. Proc. Natl. Acad. Sci. USA *106*, 16185–16190.

Anantharaman, V., Balaji, S., and Aravind, L. (2006). The signaling helix: a common functional theme in diverse signaling proteins. Biol. Direct *1*, 25.

Aravind, L., Iyer, L.M., and Anantharaman, V. (2010). Natural history of sensor domains in bacterial signaling systems. In Sensory Mechanisms in Bacteria: Molecular Aspects of Signal Recognition, S. Spiro and R. Dixon, eds. (Norwich, UK: Horizon Scientific Press).

Avila-Pérez, M., Vreede, J., Tang, Y., Bende, O., Losi, A., Gärtner, W., and Hellingwerf, K. (2009). In vivo mutational analysis of YtvA from Bacillus subtilis: mechanism of light activation of the general stress response. J. Biol. Chem. *284*, 24958–24964.

Bilwes, A.M., Alex, L.A., Crane, B.R., and Simon, M.I. (1999). Structure of CheA, a signal-transducing histidine kinase. Cell *96*, 131–141.

Capra, E.J., and Laub, M.T. (2012). Evolution of two-component signal transduction systems. Annu. Rev. Microbiol. *66*, 325–347.

Casino, P., Rubio, V., and Marina, A. (2009). Structural insight into partner specificity and phosphoryl transfer in two-component signal transduction. Cell *139*, 325–336.

Chen, V.B., Arendall, W.B., 3rd, Headd, J.J., Keedy, D.A., Immormino, R.M., Kapral, G.J., Murray, L.W., Richardson, J.S., and Richardson, D.C. (2010). MolProbity: all-atom structure validation for macromolecular crystallography. Acta Crystallogr. D Biol. Crystallogr. *66*, 12–21.

Cheung, J., and Hendrickson, W.A. (2009). Structural analysis of ligand stimulation of the histidine kinase NarX. Structure *17*, 190–201.

Christie, J.M., Reymond, P., Powell, G.K., Bernasconi, P., Raibekas, A.A., Liscum, E., and Briggs, W.R. (1998). Arabidopsis NPH1: a flavoprotein with the properties of a photoreceptor for phototropism. Science *282*, 1698–1701.

Circolone, F., Granzin, J., Jentzsch, K., Drepper, T., Jaeger, K.-E., Willbold, D., Krauss, U., and Batra-Safferling, R. (2012). Structural basis for the slow dark recovery of a full-length LOV protein from Pseudomonas putida. J. Mol. Biol. *417*, 362–374.

Cowtan, K. (2012). Completion of autobuilt protein models using a database of protein fragments. Acta Crystallogr. D Biol. Crystallogr. *68*, 328–335.

Crosson, S., and Moffat, K. (2001). Structure of a flavin-binding plant photoreceptor domain: insights into light-mediated signal transduction. Proc. Natl. Acad. Sci. USA *98*, 2995–3000.

Dago, A.E., Schug, A., Procaccini, A., Hoch, J.A., Weigt, M., and Szurmant, H. (2012). Structural basis of histidine kinase autophosphorylation deduced by integrating genomics, molecular dynamics, and mutagenesis. Proc. Natl. Acad. Sci. USA *109*, E1733–E1742.

Doublié, S. (1997). Preparation of selenomethionyl proteins for phase determination. Methods Enzymol. *276*, 523–530.

Emsley, P., and Cowtan, K. (2004). Coot: model-building tools for molecular graphics. Acta Crystallogr. D Biol. Crystallogr. *60*, 2126–2132.

Falke, J.J., and Erbse, A.H. (2009). The piston rises again. Structure *17*, 1149–1151.

Ferris, H.U., Dunin-Horkawicz, S., Hornig, N., Hulko, M., Martin, J., Schultz, J.E., Zeth, K., Lupas, A.N., and Coles, M. (2012). Mechanism of regulation of receptor histidine kinases. Structure *20*, 56–66.

Finn, R.D., Mistry, J., Schuster-Böckler, B., Griffiths-Jones, S., Hollich, V., Lassmann, T., Moxon, S., Marshall, M., Khanna, A., Durbin, R., et al. (2006). Pfam: clans, web tools and services. Nucleic Acids Res. *34*(Database issue), D247–D251.

Gao, R., and Stock, A.M. (2009). Biological insights from structures of two-component proteins. Annu. Rev. Microbiol. *63*, 133–154.

Halavaty, A.S., and Moffat, K. (2007). N- and C-terminal flanking regions modulate light-induced signal transduction in the LOV2 domain of the blue light sensor phototropin 1 from Avena sativa. Biochemistry *46*, 14001–14009.

Harper, S.M., Neil, L.C., and Gardner, K.H. (2003). Structural basis of a phototropin light switch. Science *301*, 1541–1544.

Herrou, J., and Crosson, S. (2011). Function, structure and mechanism of bacterial photosensory LOV proteins. Nat. Rev. Microbiol. *9*, 713–723.

Huang, N., Chelliah, Y., Shan, Y., Taylor, C.A., Yoo, S.-H., Partch, C., Green, C.B., Zhang, H., and Takahashi, J.S. (2012). Crystal structure of the heterodimeric CLOCK:BMAL1 transcriptional activator complex. Science *337*, 189–194.

Hulko, M., Berndt, F., Gruber, M., Linder, J.U., Truffault, V., Schultz, A., Martin, J., Schultz, J.E., Lupas, A.N., and Coles, M. (2006). The HAMP domain structure implies helix rotation in transmembrane signaling. Cell *126*, 929–940.

Kabsch, W. (1976). A solution for the best rotation to relate two sets of vectors. Acta Crystallogr. A *32*, 922–923.

Kabsch, W. (2010). XDS. Acta Crystallogr. D Biol. Crystallogr. *66*, 125–132.

Kraulis, P.J. (1991). MOLSCRIPT: a program to produce both detailed and schematic plots of protein structures. J. Appl. Cryst. *24*, 946–950.

Krissinel, E., and Henrick, K. (2007). Inference of macromolecular assemblies from crystalline state. J. Mol. Biol. *372*, 774–797.

Krug, M., Weiss, M.S., Heinemann, U., and Mueller, U. (2012). XDSAPP: a graphical user interface for the convenient processing of diffraction data using XDS. J. Appl. Cryst. *45*, 568–572.

Marina, A., Waldburger, C.D., and Hendrickson, W.A. (2005). Structure of the entire cytoplasmic portion of a sensor histidine-kinase protein. EMBO J. *24*, 4247–4259.

Mathes, T., Vogl, C., Stolz, J., and Hegemann, P. (2009). In vivo generation of flavoproteins with modified cofactors. J. Mol. Biol. *385*, 1511–1518.

Matthews, E.E., Zoonens, M., and Engelman, D.M. (2006). Dynamic helix interactions in transmembrane signaling. Cell *127*, 447–450.

McCoy, A.J., Grosse-Kunstleve, R.W., Storoni, L.C., and Read, R.J. (2005). Likelihood-enhanced fast translation functions. Acta Crystallogr. D Biol. Crystallogr. *61*, 458–464.

Möglich, A., and Moffat, K. (2007). Structural basis for light-dependent signaling in the dimeric LOV domain of the photosensor YtvA. J. Mol. Biol. *373*, 112–126.

Möglich, A., Ayers, R.A., and Moffat, K. (2009a). Design and signaling mechanism of light-regulated histidine kinases. J. Mol. Biol. *385*, 1433–1444.

Möglich, A., Ayers, R.A., and Moffat, K. (2009b). Structure and signaling mechanism of Per-ARNT-Sim domains. Structure *17*, 1282–1294.

Möglich, A., Ayers, R.A., and Moffat, K. (2010). Addition at the molecular level: signal integration in designed Per-ARNT-Sim receptor proteins. J. Mol. Biol. *400*, 477–486.

Moore, J.O., and Hendrickson, W.A. (2009). Structural analysis of sensor domains from the TMAO-responsive histidine kinase receptor TorS. Structure *17*, 1195–1204.

Moukhametzianov, R., Klare, J.P., Efremov, R., Baeken, C., Göppner, A., Labahn, J., Engelhard, M., Büldt, G., and Gordeliy, V.I. (2006). Development of the signal in sensory rhodopsin and its transfer to the cognate transducer. Nature *440*, 115–119.

Mueller, U., Darowski, N., Fuchs, M.R., Förster, R., Hellmig, M., Paithankar, K.S., Pühringer, S., Steffien, M., Zocher, G., and Weiss, M.S. (2012). Facilities for macromolecular crystallography at the Helmholtz-Zentrum Berlin. J. Synchrotron Radiat. *19*, 442–449.

Murshudov, G.N., Vagin, A.A., and Dodson, E.J. (1997). Refinement of macromolecular structures by the maximum-likelihood method. Acta Crystallogr. D Biol. Crystallogr. *53*, 240–255.

Ohlendorf, R., Vidavski, R.R., Eldar, A., Moffat, K., and Möglich, A. (2012). From dusk till dawn: one-plasmid systems for light-regulated gene expression. J. Mol. Biol. *416*, 534–542.

Parkinson, J.S., and Kofoid, E.C. (1992). Communication modules in bacterial signaling proteins. Annu. Rev. Genet. *26*, 71–112.

Purcell, E.B., Siegal-Gaskins, D., Rawling, D.C., Fiebig, A., and Crosson, S. (2007). A photosensory two-component system regulates bacterial cell attachment. Proc. Natl. Acad. Sci. USA *104*, 18241–18246.

Russo, F.D., and Silhavy, T.J. (1993). The essential tension: opposed reactions in bacterial two-component regulatory systems. Trends Microbiol. *1*, 306–310.

Schomaker, V., and Trueblood, K.N. (1968). On the rigid-body motion of molecules in crystals. Acta Crystallogr. B *24*, 63–76.

Sevvana, M., Vijayan, V., Zweckstetter, M., Reinelt, S., Madden, D.R., Herbst-Irmer, R., Sheldrick, G.M., Bott, M., Griesinger, C., and Becker, S. (2008). A ligand-induced switch in the periplasmic domain of sensor histidine kinase CitA. J. Mol. Biol. *377*, 512–523.

Sheldrick, G.M. (2008). A short history of SHELX. Acta Crystallogr. A *64*, 112–122.

Stein, N. (2008). CHAINSAW: a program for mutating pdb files used as templates in molecular replacement. J. Appl. Cryst. *41*, 641–643.

Swartz, T.E., Tseng, T.S., Frederickson, M.A., Paris, G., Comerci, D.J., Rajashekara, G., Kim, J.G., Mudgett, M.B., Splitter, G.A., Ugalde, R.A., et al. (2007). Blue-light-activated histidine kinases: two-component sensors in bacteria. Science *317*, 1090–1093.

Szurmant, H., White, R.A., and Hoch, J.A. (2007). Sensor complexes regulating two-component signal transduction. Curr. Opin. Struct. Biol. *17*, 706–715.

Tomomori, C., Tanaka, T., Dutta, R., Park, H., Saha, S.K., Zhu, Y., Ishima, R., Liu, D., Tong, K.I., Kurokawa, H., et al. (1999). Solution structure of the homodimeric core domain of Escherichia coli histidine kinase EnvZ. Nat. Struct. Biol. *6*, 729–734.

Wang, C., Sang, J., Wang, J., Su, M., Downey, J.S., Wu, Q., Wang, S., Cai, Y., Xu, X., Wu, J., et al. (2013). Mechanistic insights revealed by the crystal structure of a histidine kinase with signal transducer and sensor domains. PLoS Biol. *11*, e1001493.

Winn, M.D., Ballard, C.C., Cowtan, K.D., Dodson, E.J., Emsley, P., Evans, P.R., Keegan, R.M., Krissinel, E.B., Leslie, A.G.W., McCoy, A., et al. (2011). Overview of the CCP4 suite and current developments. Acta Crystallogr. D Biol. Crystallogr. *67*, 235–242.

Yang, X., Kuk, J., and Moffat, K. (2008). Crystal structure of Pseudomonas aeruginosa bacteriophytochrome: photoconversion and signal transduction. Proc. Natl. Acad. Sci. USA *105*, 14715–14720.

